Soft Matter

Accepted Manuscript

ROYAL SOCIETY OF CHEMISTRY

www.rsc.org/softmatter

ARTICLE TYPE www. rsc.org/xxxxxx | XXXXXXXX

Anisotropic Effective Interactions and Stack Formation in Mixtures of Semiflexible Ring Polymers

Peter Poier,*[a] Petra Bačová,[b,d] Angel J. Moreno,[b,c] Christos N. Likos[a] and Ronald Blaak[a]

Received Xth XXXXXXXXXX 20XX, Accepted Xth XXXXXXXXX 20XX
First published on the web Xth XXXXXXXXXX 200X
DOI: 10.1039/b000000x

By means of extensive computer simulations, we investigate the formation of columnar structures (stacks) in concentrated solutions of semiflexible ring polymers. To characterize the stacks we employ an algorithm that identifies tube-like structures in the simulation cell. Stacks are found both in the real system and in the fluid of soft disks interacting through the effective anisotropic pair potential derived for the rings [P. Poier *et al.*, Macromolecules, 2015, **48**, 4983-4997]. Furthermore, we investigate binary mixtures of cluster-forming and non-cluster-forming rings. We find that monodispersity is not a requirement for stack formation. The latter is found for a broad range of mixture compositions, though the columns in the mixtures exhibit important differences to those observed in the monodisperse case. We extend the anisotropic effective model to mixtures. We show that it correctly predicts stack formation and constitutes a significant improvement with respect to the usual isotropic effective description based only on macromolecular centers-of-mass.

1 Introduction

A rapidly growing body of research has been devoted to polymer rings over the last years, in different fields of mathematics, physics, chemistry and biology. The simple operation of joining permanently the two ends of a linear chain to form a topologically different object — a ring — has a dramatic effect on the properties of the former. A well-known example is their different scaling behaviour. Linear chains in θ-solvent or in polymer melts behave as ideal chains (no excluded-volume interactions) and adopt random-walk conformations[1]. Thus, their size scales with their polymerization degree N as $D_g \sim N^{1/2}$, with D_g the diameter of gyration. However, the size of isolated ideal rings (keeping the topological constraints; i.e., bond uncrossability) scales as[2–9] $D_g \sim N^{\nu_F}$, with $\nu_F \approx 0.588$ the Flory exponent. In the melt state, strongly entangled ring polymers adopt crumpled globular conformations, with an effective scaling exponent showing a crossover from $\nu \sim 0.4$ to $\nu \sim 0.33 - 0.36$ in the limit of large N[10–12]. Topological constraints have also a deep impact on the rheological properties of entangled ring polymer melts. Thus, the stress relaxation displays a long power-law decay with time, instead of the entanglement plateau followed by exponential decay observed in entangled linear chains[13,14]. Moreover, the viscosity of entangled rings exhibits a weaker dependence on the polymerization degree than their linear counterparts[14–16]. Static and dynamic properties of rings have been much less explored in the intermediate concentration regime between dilute solutions and melts. This regime is of practical relevance because of its implications in, e.g., biophysics (living cells contain concentrated solutions of biomacromolecules). Accordingly, topological interactions between ring polymers — a simple picture for chromatin loops — have been invoked for explaining the creation of chromosome territories[17–22].

The investigation of ring polymer properties in the semidilute regime can be facilitated by using a coarse-graining approach. In this methodology the internal degrees of freedom of the polymer (i.e., the monomer coordinates) are replaced by a reduced set of suitably-chosen effective coordinates. In this way, each real macromolecule is substituted by a single-particle (represented by the effective coordinates) interacting with the others through an effective potential. The microscopic information of the real macromolecule determines the form of the effective potential. This potential is generally *ultrasoft*[23] since, unlike hard or quasi-hard objects, macromolecules can interprenetrate at a moderate energetic cost. Simulation of the fluid of ultrasoft particles provides an economical route to investigate properties of the real macromolecular solution. Indeed, by using the effective coordinates, most of the degrees of freedom are removed and the computational effort is largely reduced.

The methodology of coarse-graining is well-established and has found successful application in, e.g., polymer chains[24–26],

[a] *Faculty of Physics, University of Vienna, Boltzmanngasse 5, A-1090, Vienna, Austria, E-mail: peter.poier@gmail.com*
[b] *Centro de Física de Materiales (CSIC-UPV/EHU) and Materials Physics Center MPC, Paseo Manuel de Lardizabal 5, E-20018 San Sebastián, Spain*
[c] *Donostia International Physics Center, Paseo Manuel de Lardizabal 4, E-20018 San Sebastián, Spain*
[d] *Institute of Applied and Computational Mathematics (IACM), Foundation for Research and Technology Hellas (FORTH), GR-71110 Heraklion, Greece*

star polymers[27–30], star-shaped polyelectrolytes[31,32], dendrimers[33–35], block copolymers[36–38] and rings[39,40], among others. The dramatic effect of the ring topology on the polymer properties with respect to those for the case of linear chains becomes again evident in the effective potential. Linear chains interact through effective Gaussian potentials[24,25]. However, for ring polymers a non-Gaussian potential is found, which can even show a minimum at zero distance[39,40] and includes a contribution from the *topological-potential*[41]. The effective attraction associated to this minimum is a direct consequence of the usual configurations of two rings with coincident or very close centers-of-mass: in such configurations one of the rings 'opens up' to be threaded by the other one[39,42]. The effective interaction can lead to a striking feature in rings with, *purely repulsive*, excluded volume interactions between the monomers. Namely, a cluster phase can emerge in the case of *semiflexible* rings[40], which unlike flexible rings[12,39], only show a weak shrinkage with increasing concentration, facilitating full interpenetration[40].

The identification of the relevant degrees of freedom is an essential part in the design of an effective model[23,43]. In many situations of interest, the macromolecule is represented as a point particle at the position of a selected monomer (e.g., the central one in a star polymer) or more generally the position of the macromolecular center-of-mass. If the latter is chosen as the effective coordinate, the effective ultrasoft potential is *bounded*, since the centers-of-mass of two macromolecules can coincide at a finite energetic cost. Hence the ultrasoft particles are fully penetrable. Because of their simplicity, this family of ultrasoft particles has motivated a huge amount of theoretical and computational investigations, leading to the discovery of new structural and dynamic scenarios with potential realization in solutions of real macromolecules[44–61].

The choice of the center-of-mass position as the single relevant effective coordinate results by construction in, rotationally-averaged, *isotropic* effective potentials. However, this approach is not justified for every macromolecule, as e.g., in the case of *semiflexible* ring polymers. In ref.[40] semiflexible rings were coarse-grained to ultrasoft particles interacting by an isotropic potential, dependent only on the relative distance between centers-of-mass. In an intermediate range of N-values, corresponding to ratios of contour-to-persistence length $N/s_p \sim 6.7$, clustering of the rings was observed both in the real monomer-resolved system and in the isotropic effective model. This was recognized by a peak at distance $r = 0$ in the radial distribution function $g(r)$ of the centers-of-mass. However, clustering in the real system was markedly *anisotropic*. The cluster phase in the real system was formed by disordered columns ('stacks') of oblate rings, penetrated by bundles of elongated prolate rings. Though for small N, $N/s_p \sim 2.7$, interpenetration and clustering was negligible ($g(r \to 0) \ll 1$) due to excluded volume, anisotropic stacking of the rings was still observed. These features were not captured by the effective isotropic potential, which indeed did not take into account the orientation-dependent character of the real interactions, and led to the formation of isotropic clusters. Rings with high bending stiffness or few monomers have a strong tendency to orient with respect to other rings in their proximity. Thus, the energetic cost paid for mutually approaching two stiff rings to a fixed (small) separation between their centers-of-mass is highly dependent on their relative orientation. The absence of this feature in the effective isotropic model did not only result in the failure to predict the anisotropic character of the stacks and clusters. It also resulted in a poor description, in dense solutions, of rotationally-averaged static correlation functions as $g(r)$.

In order to improve the description of the real monomer-resolved system, an *anisotropic* effective model for semiflexible ring polymers has been introduced[62]. In that model, the effective particles are defined as soft disk-like molecules. These were represented not only by the positions of their centers-of-mass, but also by the direction in which their faces were oriented. A considerable improvement in the description of the monomer-resolved system was achieved by the effective anisotropic model for small-N (non cluster-forming) and intermediate N (cluster-forming). Namely, in comparison to the isotropic model, it provided a much better description of $g(r)$, and was applicable over a broader density range. It also accounted for the orientational correlations between neighbouring rings. The isotropic model provided, however a better description than the anisotropic one in the case of (non cluster-forming) long rings (large N, $N/s_p \sim 13.3$). This was attributed to the overestimation of the orientational effects in the interactions between long rings, which are much more deformable than those with small or intermediate N and the same stiffness. We restrict ourselves to unknotted ring polymers in this work, although the same approach could also be used to derive the effective potential between ring polymers containing knots, which can can have a significant influence on both the structural as well as dynamic properties of the system[63]. In ref.[64,65] Heinemann et al. follow a similar approach showing that the anisotropy in the effective interactions of the molecule coronene plays a crucial role in its structural properties.

In this article we investigate whether stacking is reproduced by the anisotropic effective model, and how the results compare with respect to the real monomer-resolved system. To this end, we introduce an algorithm to define a stack of ring polymers, and compare the distribution of stack sizes in the effective and monomer-resolved systems. Furthermore, we examine whether monodispersity is required for the occurrence of stacks, by investigating binary mixtures of rings of different sizes. In particular, we simulate mixtures of rings with intermediate and small N, which form and do not form, respectively, cluster phases in the monodisperse case. We find that

stacking is resilient to polydispersity, persisting even in mixtures with 50 % of non cluster-forming rings. The article is organized as follows. In Section 2 we summarize model and simulation details[40] of the monomer-resolved and monodisperse effective system. In Section 3 we introduce the algorithm for identifying stacks. In Section 4 we summarize the method to derive the effective potentials[62]. In Section 5 we characterize stacks in the monodisperse systems. In Section 6 we show results for effective potentials corresponding to the cross-interactions between small and intermediate rings. In Sections 7 and 8 we show results for the binary mixtures and characterize, respectively, static correlations and stacks. We compare the obtained results for the real mixtures and the effective systems. Conclusions are given in Section 9.

2 Model and Simulation Details

The monomer-resolved system consists of bead-spring rings. Non-bonded interactions between monomers are given by the cut-and-shifted Lennard-Jones (LJ) potential[66]:

$$V_{\mathrm{LJ}}(r) = \begin{cases} 4\varepsilon\left[\left(\frac{\sigma}{r}\right)^{12} - \left(\frac{\sigma}{r}\right)^{6} + \frac{1}{4}\right] & \text{if } r < 2^{1/6}\sigma; \\ 0 & \text{if } r \geq 2^{1/6}\sigma. \end{cases} \quad (1)$$

This potential is purely repulsive, accounting then for monomer excluded volume interactions. Bonded monomers also interact through a FENE potential[66]:

$$V_{\mathrm{FENE}}(r) = -\frac{kR_0^2}{2}\ln\left[1 - \left(\frac{r}{R_0}\right)^2\right]. \quad (2)$$

Rigidity is introduced via the bending potential

$$V_{\mathrm{bend}}(\theta) = \kappa(1-\cos\theta)^2, \quad (3)$$

where θ is the angle between two consecutive bond vectors. We choose $\varepsilon = k_BT$, $k = 30k_BT/\sigma^2$, $R_0 = 1.5\sigma$ and $\kappa = 30k_BT$, where k_B is the Boltzmann constant and T the temperature. All simulations are done at $k_BT = 1$. In what follows absolute distances will be given in units of the LJ diameter σ. The characteristic ratio C_∞ and persistence length bs_{p} of the model are estimated[62] as $C_\infty \sim 15$ and $bs_{\mathrm{p}} \sim 7.5$, where b is the bond length ($b \sim 0.97$). We performed standard Langevin dynamics simulations to investigate solutions of the monomer-resolved rings at different densities. We define the reduced density as $\rho^* = nV^{-1}D_{\mathrm{g0}}^3$, with n the number of rings, V the volume of the simulation box, and D_{g0} the diameter of gyration of the ring at infinite dilution ($\rho^* = 0$). The overlap density is defined as $\rho^* = 1$ and represents the concentration at which the peripheria of the rings start to overlap. The investigated solutions covered a broad range of densities from high dilution to several times the overlap density.

The effective isotropic and anisotropic potentials were derived (see below) from the distribution functions of the relative distances (in both cases) and the relative orientations (in the anisotropic case). Such distributions were sampled from simulations of two isolated rings at different relative distances. Bias Monte Carlo and molecular dynamics methods were used for efficient sampling[40,62]. The solutions of the ultrasoft particles, interacting through the effective isotropic or anisotropic potentials, were simulated by standard Langevin and Monte Carlo dynamics. As in the monomer-resolved case, they covered a broad range of densities from high dilution to several times the overlap density. Further simulation details are given in refs.[40,62].

3 Algorithm for the Identification of Stacks

Now we describe the algorithm to identify the stacks of rings. Defining a condition for two rings to be neighbour particles in a stack is sufficient to identify all the stacks in the system. To identify a stack we randomly choose some ring A and start with a set that contains only this ring as a member. We continue to extend the set by the neighbours of its members until no new rings are added, and the set thus corresponds to the stack which contains the ring A. We repeat the procedure for the rings that are not part of any stack yet and thus gradually identify the stacks in the system.

We will formulate the condition for two rings to be neighbours in a stack in terms of the effective coordinates of the rings, defined in ref.[62], which are accessible in both the effective and the monomer-resolved simulations. Let us consider two rings with the effective coordinates $(\mathbf{R}^{(1)}, \mathbf{d}^{(1)})$ and $(\mathbf{R}^{(2)}, \mathbf{d}^{(2)})$. $\mathbf{R}^{(i)}$ refers to the center-of-mass of the respective ring and $\mathbf{d}^{(i)}$ to its normalized director ($|\mathbf{d}^{(i)}| = 1$). The director is defined along the direction of the smallest eigenvalue of the gyration tensor of the ring. Thus, for an ideally flat ring the director is perpendicular to the plane of the ring. We define $\mathbf{r} \equiv \mathbf{R}^{(2)} - \mathbf{R}^{(1)}$ as the relative vector between the centers-of-mass of the rings. We formulate our criteria for identifying stacks such that they contain rings that form tube-like structures. While it is possible that other rings interpenetrate these tubes, we will not aim at identifying them as members of the stack. Therefore, the first condition for two rings to be neighbours in a stack is that their directors are almost parallel:

$$|\mathbf{d}^{(1)} \cdot \mathbf{d}^{(2)}| > 1 - \Delta\gamma, \quad (4)$$

where the parameter $\Delta\gamma$ is fixed to some value (see below) and quantifies how much the directors of two neighbours in a stack can deviate from a perfectly parallel orientation ($\Delta\gamma = 0$). Furthermore, the centers-of-mass of neighbours in a stack must be close to each other. We differentiate between the distance in the $\mathbf{d}^{(1)}$ direction, which is given by $|\mathbf{r} \cdot \mathbf{d}^{(1)}|$, and

in the direction orthogonal to it, which can be computed as $|\mathbf{r}-\mathbf{d}^{(1)}(\mathbf{r}\cdot\mathbf{d}^{(1)})|$. We restrict both of these distances independently:

$$|\mathbf{r}\cdot\mathbf{d}^{(1)}| < v_{||}, \tag{5}$$

$$|\mathbf{r}-\mathbf{d}^{(1)}(\mathbf{r}\cdot\mathbf{d}^{(1)})| < v_{\perp}. \tag{6}$$

For perfectly parallel rings $v_{||}$ controls the maximum distance between the ring surfaces, while $v_{\perp}$ sets how much misalignment between the centers-of-mass of the two rings is accepted. Conditions (4) - (6) must be simultaneously fulfilled.

It is arbitrary which ring has the label 1 and therefore the result of whether the two rings are neighbours in a stack must not depend on it. However, conditions (5)-(6) have an explicit dependence on $\mathbf{d}^{(1)}$. In order to restore the $1 \leftrightarrow 2$ symmetry, we also classify rings 1 and 2 as belonging to the same stack if the conditions in (5)-(6) are satisfied for $\mathbf{d}^{(1)} \rightarrow \mathbf{d}^{(2)}$. Since, for small $\Delta\gamma$, the condition (4) requires $\mathbf{d}^{(1)}$ and $\mathbf{d}^{(2)}$ to be similar, the change $\mathbf{d}^{(1)} \rightarrow \mathbf{d}^{(2)}$ just slightly modifies the numerical values of the left sides of conditions (4)-(6), which are still fulfilled.

The parameters $\Delta\gamma$, $v_{||}$ and $v_{\perp}$ have to be set by hand. If one only wants the algorithm to identify a stack if the rings form perfect tubular structures, one has to choose $\Delta\gamma, v_{\perp} \rightarrow 0$, with some finite $v_{||}$, quantifying by how much the rings forming the tube can be separated. We have chosen finite values for $\Delta\gamma$ and $v_{\perp}$, since the stacks formed by the rings in simulations always exhibit imperfections with respect to a perfect tube-like arrangement. We use $v_{||} = 3\sigma$, $v_{\perp} = 2.5\sigma$, $\Delta\gamma = 0.1$ for the identification of stacks of rings with $N = 50$ monomers, and $v_{||} = 5\sigma$, $v_{\perp} = 5\sigma$, $\Delta\gamma = 0.1$ in the case of larger rings with $N = 100$ monomers. This choice of parameters is justified a posteriori, since it has resulted in the identification of stacks that are compatible with our intuitive notion of tube-like structures. The stack-identification algorithm together with this choice of parameters therefore provides an unambiguous definition of stacks of ring polymers. We have to emphasize that this definition is not the only sensible one, and that the results obtained with a 10% variation in the parameters $\Delta\gamma$, $v_{||}$ and $v_{\perp}$ were qualitatively identical.

Using this algorithm we can determine the stacks in configurations of anisotropic effective, as well as monomer-resolved systems. As shown below, for both levels of description we observe the formation of long columns at sufficiently high densities. On the other hand, in the isotropic effective model stacks are never observed, confirming that in order to describe the system at high densities, at least at a qualitative level, the introduction of anisotropy is essential. It is interesting to note that the absence of stacks in the isotropic effective model is not self-evident, since there exist other systems where the interactions between particles are also isotropic and *stacks*, i.e. linear clusters, are formed[67,68].

4 Derivation of the Effective Potentials

In refs.[40,62] we derived isotropic and anisotropic effective potentials for the description of *monodisperse* systems of semiflexible ring polymers. One can extend these models for the description of mixtures, by introducing interaction potentials between different ring types. In this work, we will limit ourselves to mixtures of rings with $N = 20$ and $N = 50$ monomers, but an extension to other binary, or multicomponent mixtures is straightforward. As discussed in ref.[62] this corresponds to rings with a contour to persistence length ratio N/s_p of ~ 2.7 and ~ 6.7 respectively (rings of $N = 100$ to be discussed below have $N/s_p \sim 13.3$). The diameter of gyration at infinite dilution of the rings with $N = 20, 50$ and 100 monomers is $\mathrm{D_{g0}} = 5.9\sigma$, 13σ and 21.5σ respectively.

To determine the effective interaction potential between different ring types, we follow a similar procedure to that reported in ref.[62] for the case of identical rings. In particular, we carry out simulations of a system of two ring polymers. We then determine $\mathrm{P}(r, \cos\theta_1, \cos\theta_2, \varphi)$, which is the probability density to find the two rings at a certain distance and relative orientation with respect to each other. The arguments of P refer to the effective coordinates defined in Eq. (6) in ref.[62]. Namely, r is the distance between the centers-of-mass of the two rings (denoted as 1 and 2), and θ_i is the angle between the vector $\mathbf{r}$ joining the centers-of-mass and the director $\mathbf{d}^{(i)}$ of the i-ring. The angle φ is the angle between $\mathbf{d}_{\perp}^{(1)}$ and $\mathbf{d}_{\perp}^{(2)}$, which are the components of $\mathbf{d}^{(1)}$ and $\mathbf{d}^{(2)}$ perpendicular to $\mathbf{r}$. It is important to note at this point that if the two rings are not identical (different N), the distribution P is not invariant under the exchange of $\cos\theta_1$ and $\cos\theta_2$, since these now refer to directors of nonequivalent rings. For this reason also the effective interaction between different ring types loses the $\cos\theta_1 \leftrightarrow \cos\theta_2$ symmetry. We then compute the anisotropic pair correlation function as

$$\mathrm{g}(r, \cos\theta_1, \cos\theta_2, \varphi) = \frac{\mathrm{P}(r, \cos\theta_1, \cos\theta_2, \varphi)}{\mathrm{P_{id}}(r, \cos\theta_1, \cos\theta_2, \varphi)}, \tag{7}$$

where $\mathrm{P_{id}} \sim r^2$ is the probability density for an ideal gas of (non-interacting) effective particles. To determine $\mathrm{P}(r, \cos\theta_1, \cos\theta_2, \varphi)$ we employed umbrella sampling. Details of the simulations were explained in section 3 in ref.[62]. The effective anisotropic potential is obtained as

$$\beta \mathrm{V_{eff}}(r, \cos\theta_1, \cos\theta_2, \varphi) = -\ln\left[g(r, \cos\theta_1, \cos\theta_2, \varphi)\right]. \tag{8}$$

with $\beta = (k_B T)^{-1}$. In the isotropic case, the procedure to obtain the effective potential between different types of rings is identical to the former. As in the monodisperse case, one can deduce the radial distribution function $\mathrm{g^{iso}}(r)$ by averaging over $\cos\theta_{1,2}$ and φ in the anisotropic pair correlation function, and obtains the isotropic interaction potential as $\beta \mathrm{V_{eff}^{iso}}(r) = -\ln \mathrm{g^{iso}}(r)$.

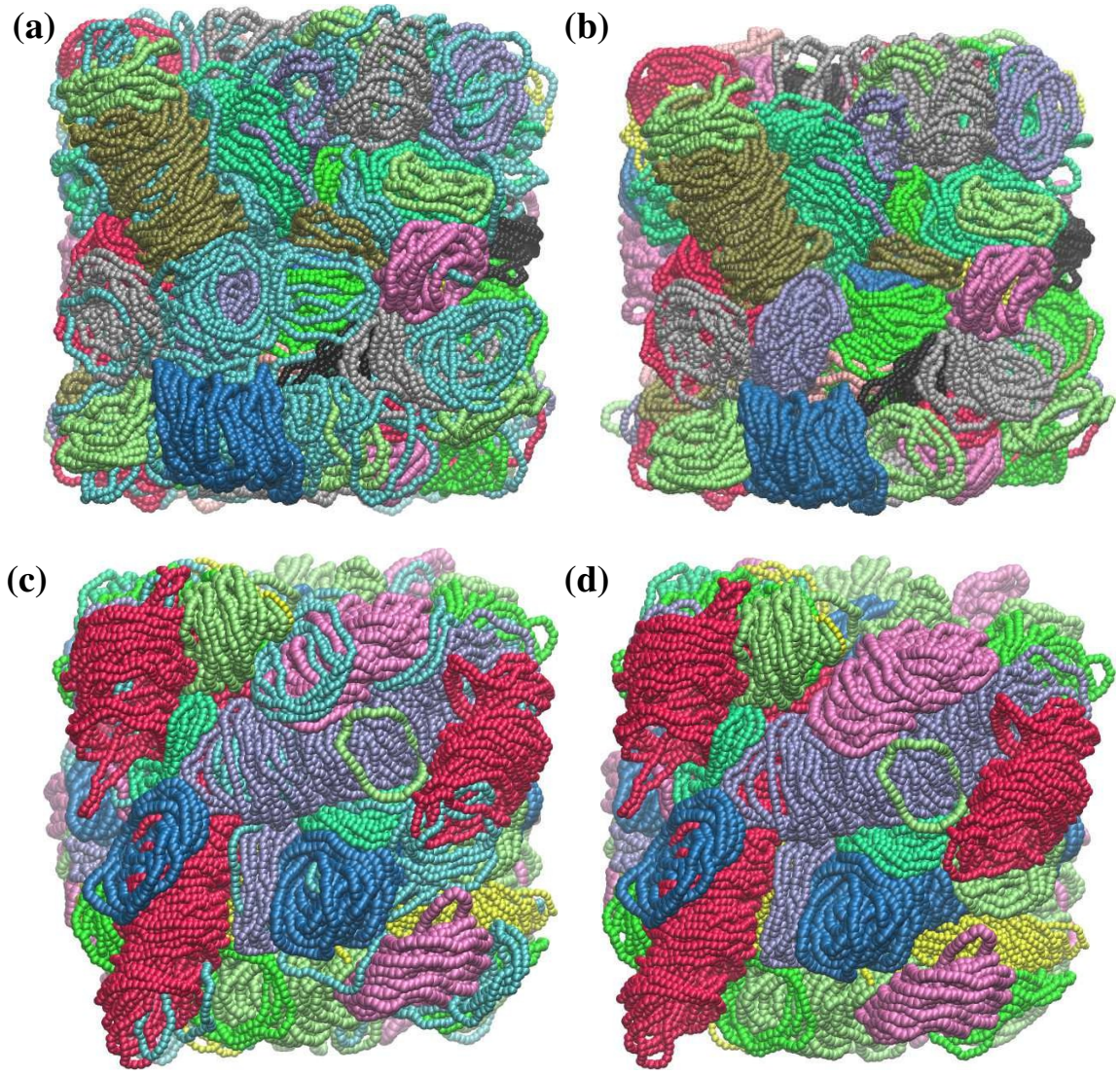

Fig. 1 Snapshots of a monomer-resolved system of ring polymers with $N = 50$ monomers. Rings belonging to the same stacks are dyed with identical colors. Turquoise polymers belong to a stack with less than 5 members. Snapshots **(a), (b)** are taken from a simulation at density $\rho^* = 16.3$, while **(c), (d)** are for the density $\rho^* = 20.0$. The snapshots **(a), (c)** contain all the particles simulated, while turquoise rings are not shown in **(b), (d)**.

5 Formation of Stacks in Monodisperse Systems

Using the previously described algorithm for the identification of stacks, we have analyzed configurations of monomer-resolved and effective simulations of monodisperse systems of ring polymers with $N = 50$ and $N = 100$ monomers. In figure 1 we present simulation snapshots of a monomer-resolved monodisperse system containing rings with $N = 50$ monomers. The snapshots are both at high densities, namely $\rho^* = 16.3$ and 20.0 respectively. In the snapshots, rings belonging to the same stack have identical colors. Rings which are not part of any stack or part of a stack that contains less than 5 rings are painted in turquoise. The particular choice of 5 allows us to discard all temporarily formed small groups of rings. For every density, we display two snapshots, where in the first all the rings are shown while in the second the turquoise rings are hidden for clarity. It can be seen that already at the lower density the majority of the stacks contain more than 5 rings and at the larger density one can spot several long columns that extend throughout the whole simulation box. For clarity, rings are always depicted as a whole and therefore individual monomers can lie outside of the periodic boundaries of the simulation box, while the center-of-mass of a ring is always within the boundaries. Some of the columns continue over the periodic boundary conditions. Columns can grow very long at large densities, however they do not display any orientational order within the simulation time.

In figure 2 analogous snapshots of the anisotropic effective system are shown. At the density $\rho^* = 20$ one can see some stacks containing 20 or more rings, but the length of the columns is reduced with respect to the corresponding monomer-resolved system. Comparing the snapshots of the effective model with the ones in figure 1 one sees that the interpenetration of the rings is disfavored in the effective case. The reason for this might be that in the effective simulation an individual ring, which is squeezed within a stack that stands orthogonal to it, pays a very high free energy penalty, since one adds up pair terms of effective potential for every interpenetrated ring in the stack. However, in the monomer-resolved simulation the deformation energy to squeeze a ring within one or several rings does not differ by such a big amount and the energy barrier for the interpenetration of stacks is therefore lower. This feature was already indirectly observed in figure 11(b) in ref.[62], where it was found that the directors of neighboring rings are more likely to be orthogonal in the monomer-resolved than in the effective simulation. This can also be related to the enhanced stack size in the monomer-resolved simulation, since interpenetration enhances the directionality of the stacking and therefore also the formation of long columns. In addition, interpenetration should enhance the alignment of the centers-of-mass of the stacked rings, and one can indeed see that the columns in the monomer-resolved snapshots are straighter than in the effective ones. By increasing the density to $\rho^* = 30$, the length of the columns formed by the soft disks increases significantly and the stack length distribution becomes comparable to the one observed at $\rho^* = 20$ in the monomer-resolved simulation, while the center-of-mass alignment of the disks within a stack is still reduced with respect to the monomer-resolved simulation.

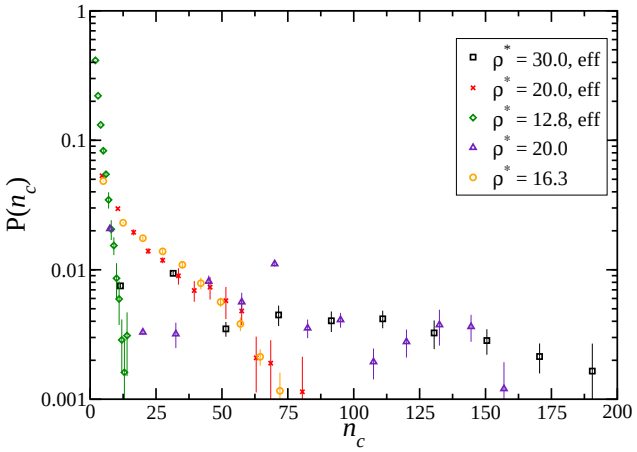

Fig. 3 Probability distribution, $P(n_c)$, for a ring to be part of a stack with n_c members for different densities in anisotropic effective and monomer-resolved simulations. Results for the former are indicated by *eff* in the legend, on which the density ρ^* is also quoted.

In figure 3 we have compared the distribution of stack lengths at different densities. The plotted function $P(n_c)$ gives the probability that a randomly chosen ring is part of a stack with n_c members. To compute $P(n_c)$ we have analyzed several configurations, which are separated by 10^6 MD steps in the case of the monomer-resolved system and by 2×10^4 MC steps for the anisotropic effective system. Errorbars have been computed assuming that the $P(n_c)$ distributions of different configurations are uncorrelated. The small errorbars for the $P(n_c)$ distribution evaluated for the highest simulated densities might underestimate the *real* error, since the cluster dynamics becomes glassy at high densities (for more details see ref.[61]) and the assumption that the analyzed configurations are uncorrelated is therefore not valid. While the formation of stacks is obviously enhanced in the monomer-resolved simulation, the effective model eventually shows the same stack length distribution at higher densities. One can for instance see that the stack size distributions for the soft disk model at $\rho^* = 20$ and $\rho^* = 30$ are almost identical to those obtained

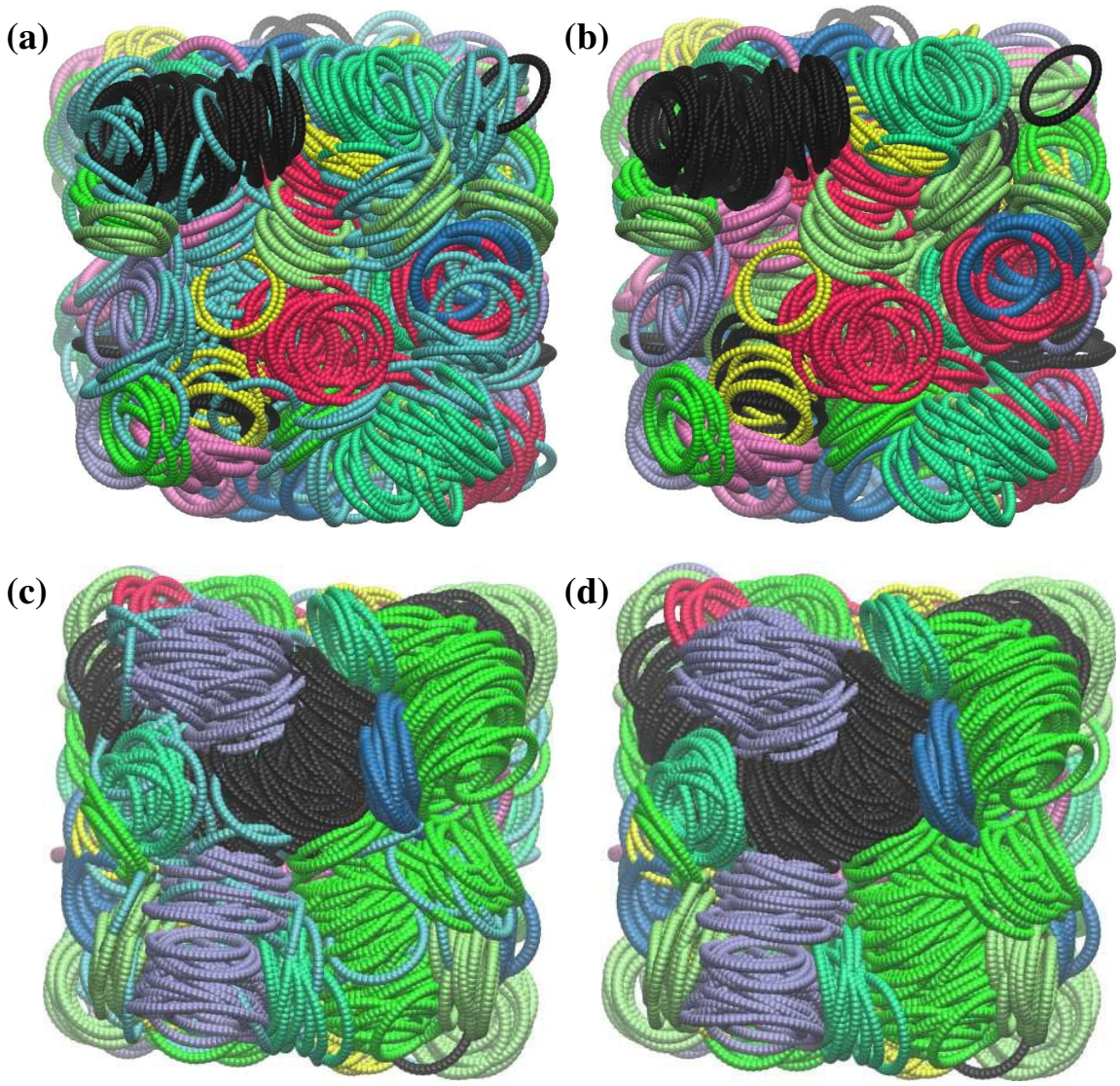

Fig. 2 Snapshots of a simulation of soft disks, representing ring polymers with $N = 50$ monomers. The effective particles are visualized by perfect circles of radius $R_{g0} = 6.5\sigma$, with director vectors and centers-of-mass identical to those of the corresponding effective particles. R_{g0} is the radius of gyration of the represented rings at zero density. Rings belonging to the same stack are dyed with identical colors. Turquoise rings belong to a stack with less than 5 members. Snapshots **(a), (b)** are taken from a simulation at density $\rho^* = 20.0$, while **(c), (d)** are for the density $\rho^* = 30.0$. The snapshots **(a), (c)** contain all the particles simulated, while turquoise rings are not show in **(b), (d)**.

for the monomer-resolved model at $\rho^* = 16.3$ and $\rho^* = 20.0$, respectively. These results demonstrate that the anisotropic effective model is a significant improvement over an isotropic model, where the formation of stacks is excluded in first place. Although quantitative agreement with the monomer-resolved simulation cannot be achieved, the formation of stacks is correctly predicted and even the stack-size distribution is similar to that of a monomer-resolved simulation at a lower density.

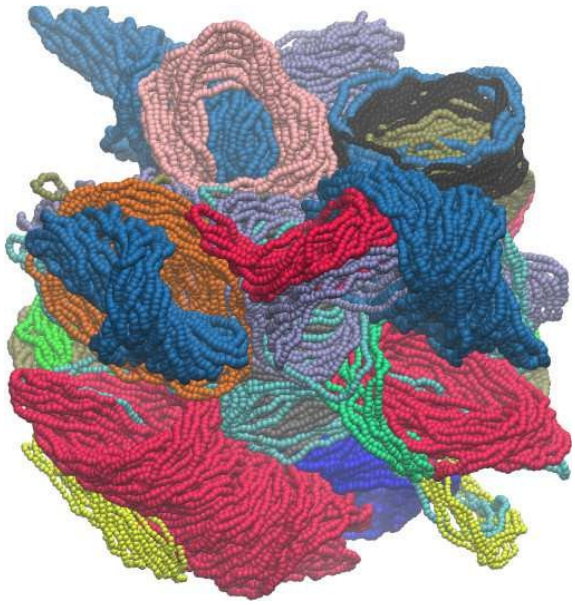

Fig. 4 Snapshot of a monomer-resolved system of ring polymers with $N = 100$ monomers at density $\rho^* = 44.2$. Rings belonging to the same stack are dyed with identical colors. Turquoise polymers belong to a stack with less than 5 members.

Analogously we have analyzed configurations of systems with $N = 100$ monomers. In ref.[62] we found that for these long rings the agreement of the soft disk model with the real system was worse than in the case of the smaller ring sizes $N = 20$ and $N = 50$. The anisotropic model even provided a worse description than the isotropic one for the correlation functions of $N = 100$. We attributed this to the fact that the long rings have a larger ratio between contour and persistence length, and are thus more easily deformed. At higher densities, they therefore acquire collapsed configurations that significantly deviate from the most probable ones in the infinitely dilute limit, at which the effective interactions have been derived. In this work we have performed new simulations of the real system for $N = 100$, investigating higher densities than in ref.[62]. As can be seen in figure 4, if one continues to increase the density in the monomer-resolved simulations, the rings again favor configurations which are expanded and much closer to disk-like shapes than those found at lower densities. The reason for this might be that if the volume per ring becomes very small, the system prefers a more optimally packed state, where individual rings have more space to fluctuate. At some density a configuration of expanded rings, which are packed within columns, is apparently the best compromise for the system, and in this state the individual rings are again more disk-like.

As a consequence the configurations of the anisotropic and the monomer-resolved system at high densities are qualitatively similar, and long columns are formed in both cases. For the effective system, the stacks also orient themselves with respect to each other, while this does not happen to the same extent in the monomer-resolved simulation. Therefore, for high densities the disk-like nature of the effective model is again an appropriate description for the long rings, at least at a qualitative level.

6 Effective Model for Binary Mixtures

We have computed the anisotropic effective correlation function $\mathrm{g}(r, \cos\theta_1, \cos\theta_2, \varphi)$ between two stiff ring polymers containing $N = 20$ and $N = 50$ monomers at infinite dilution, which is related to the interaction potential between effective particles of different types via equation (8). The four-dimensional pair correlation function is difficult to visualize, however we can consider a reduced version of this function:

$$\mathrm{g}(r, \mathbf{d}^{(1)} \cdot \mathbf{d}^{(2)}) = \frac{\mathrm{P}(r, \mathbf{d}^{(1)} \cdot \mathbf{d}^{(2)})}{\mathrm{P_{id}}(\mathrm{r}, \mathbf{d}^{(1)} \cdot \mathbf{d}^{(2)})}. \tag{9}$$

Here $\mathrm{P}(r, \mathbf{d}^{(1)} \cdot \mathbf{d}^{(2)})$ is the probability distribution to find two isolated ring separated by a distance r and with a scalar product $\mathbf{d}^{(1)} \cdot \mathbf{d}^{(2)}$ between their directors, while $\mathrm{P_{id}} \sim r^2$ gives the same distribution for two non-interacting rings. In figure 6 we present results for the function

$$\mathrm{G}(r, \mathbf{d}^{(1)} \cdot \mathbf{d}^{(2)}) = \frac{\mathrm{g}(r, \mathbf{d}^{(1)} \cdot \mathbf{d}^{(2)})}{\mathrm{g^{iso}}(r)}, \tag{10}$$

which gives the probability distribution of the scalar product between the directors of two isolated rings at a fixed mutual distance r. The abscissa in the plot is given by $r/\mathrm{D_{g0}}$, where $\mathrm{D_{g0}}$ refers to the diameter of gyration of the $N = 50$ rings at infinite dilution. In the following, $r/\mathrm{D_{g0}}$ will always refer to the distance normalized by the diameter of gyration of the larger rings in the mixture. Compared to the $\mathrm{G}(r, \mathbf{d}^{(1)} \cdot \mathbf{d}^{(2)})$ of identical ring polymers[62], the anisotropy is significantly reduced. In particular the distribution of $\mathbf{d}^{(1)} \cdot \mathbf{d}^{(2)}$ is almost flat for small distances r, where the directors had a tendency to be orthogonal with respect to each other in the case of identical rings. For $r \approx 0.4\mathrm{D_{g0}}$ the directors do have a tendency to orient parallel, but the extent of this is much weaker than for identical $N = 50$ and even $N = 100$ rings.

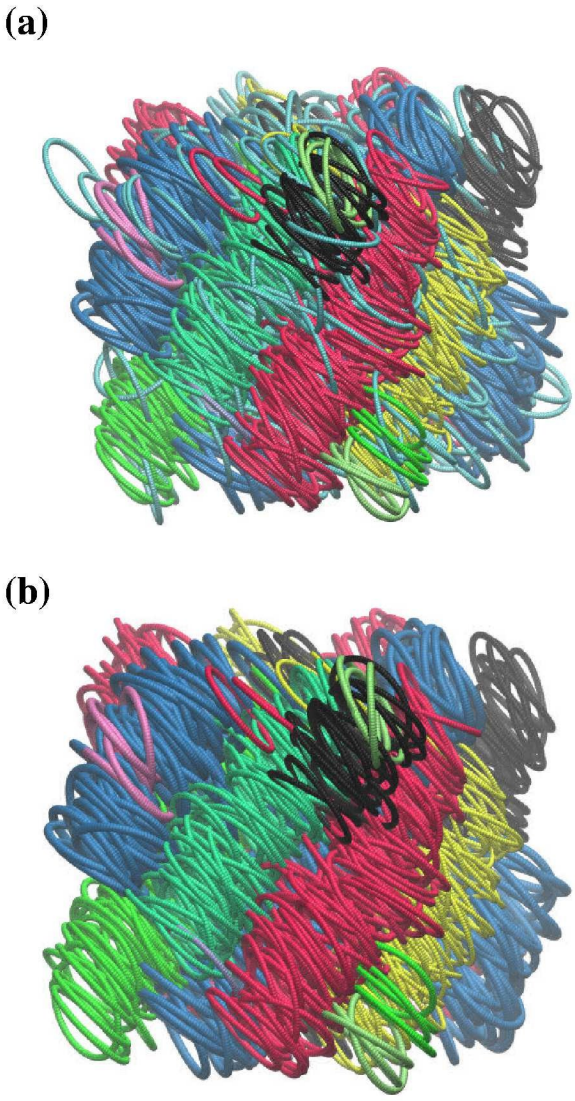

Fig. 5 Snapshots of the soft-disk model for rings of $N = 100$, at density $\rho^* = 29.0$. The effective particles are visualized by perfect circles of radius $R_{g0} = 10.8\sigma$, with director vectors and centers-of-mass identical to those of the corresponding effective particles. R_{g0} is the radius of gyration of the represented rings at zero density. Rings belonging to the same stack are dyed with identical colors. Turquoise rings belong to a stack with less than 5 members. Snapshot **(a)** contains all the particles simulated, while turquoise rings are not shown in **(b)**.

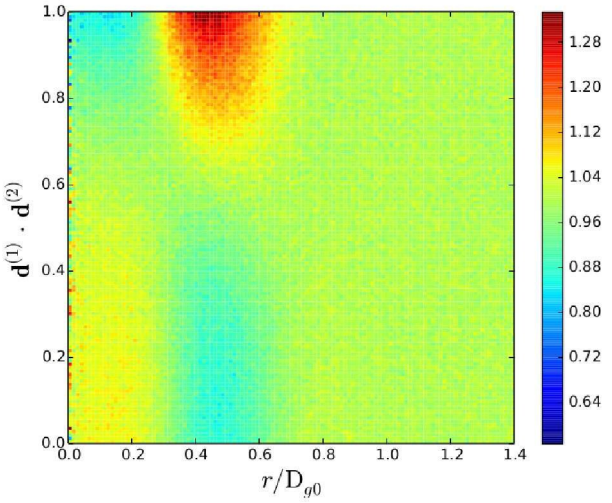

Fig. 6 Infinite-dilution limit of the quantity $G(r, \mathbf{d}^{(1)} \cdot \mathbf{d}^{(2)})$, which quantifies the distribution of the scalar product between directors for different values of r. We visualize this distribution between rings of size $N = 20$ and $N = 50$.

In figure 7, we present the rotationally averaged, isotropic effective potential, and the anisotropic potentials evaluated for three fixed orientations of the rings (see legend). The analogous plots for the interactions between identical rings have been displayed in figure 4 in ref.[62], where also the precise meaning of the three fixed orientations is described in more detail. There is now almost no difference between $V_{|-}$ and V_{--}, which both remain very low for all distances r. As in the case of identical rings, $V_{||}$ rises significantly at intermediate distances, when the contours of the rings start to overlap, but different to the case of identical rings, $V_{|-}$ is as low as the other potentials for small distances r. This is quite intuitive since the smaller ring can easily fit inside the larger one, irrespective of its orientation. In general, the interaction potentials between different rings are significantly weaker than for identical rings.

7 Correlation functions in binary mixtures

We have carried out simulations of binary mixtures of rings with $N = 20$ and $N = 50$ monomers, employing the methods described in Refs.[40,62]. For the reduced density in a mixture of rings, we use the following definition:

$$\rho^* \equiv \frac{\sum_i n^{(i)} \left(\mathrm{D}_{\mathrm{g0}}^{(i)}\right)^3}{V}, \qquad (11)$$

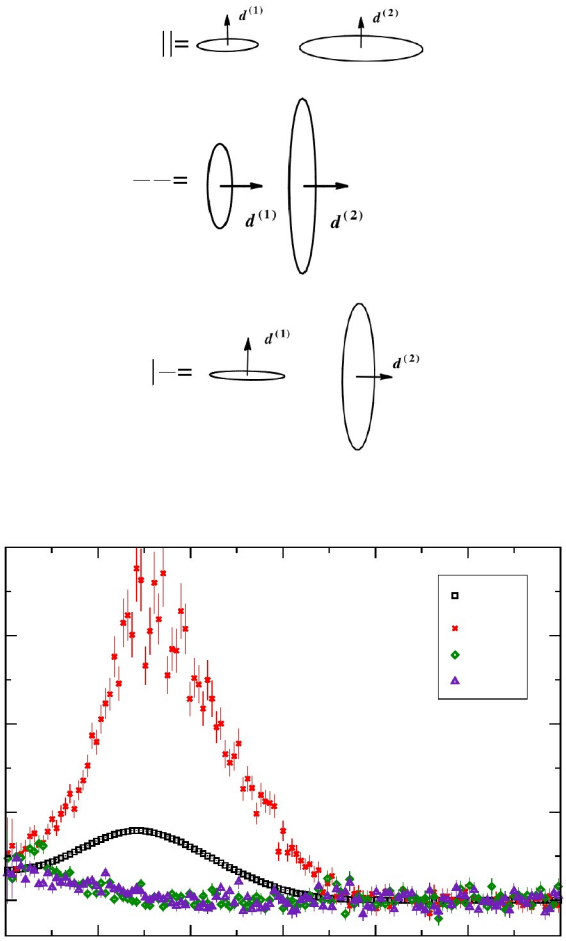

Fig. 7 The pair potential in the isotropic effective model ($\beta V_{\rm eff}^{\rm iso}(r) = -\ln g^{\rm iso}(r)$) and for three different, fixed orientational degrees of freedom (through eq 8). These are potentials between rings with $N = 20$ and $N = 50$ monomers. A sketch illustrates the ||, —— and |— configurations.

where V is the volume of the simulation box, $n^{(i)}$ the number of rings of type i, and $D_{g0}^{(i)}$ the diameter of gyration of the respective rings at infinite dilution. We first concentrate on a system with 1143 $N = 20$ and the same number of $N = 50$ rings, to which we will refer to as the 1:1 mixture. Radial distribution functions of such a system at density $\rho^* = 1.2$ are presented in figure 8. The plot shows that at the density $\rho^* = 1.2$ both the anisotropic as well as the isotropic effective model (derived at infinite dilution[62]) are in excellent agreement with the monomer-resolved simulation results, which implies that many-body effects are very small and that orientation-specific correlations are weak.

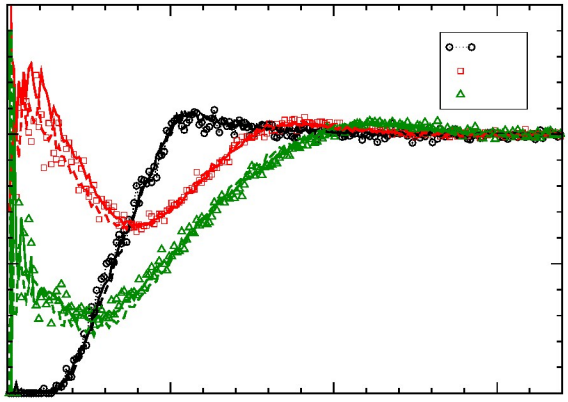

Fig. 8 Pair correlation functions, at density $\rho^* = 1.2$, for the 1:1 mixture, in the full monomer-resolved simulation (symbols), the anisotropic effective model (solid lines) and the isotropic effective model (dashed lines). Different colors refer to the pair correlation function between different types of rings (see legend).

In figures 9, 10 and 11 we show the same correlation functions at the higher densities $\rho^* = 3.9$, 10.0 and 15.7. At $\rho^* = 3.9$ the results for $g_{20,20}$ and $g_{50,50}$ are still in good agreement with the monomer-resolved simulations, while the results of the isotropic model deviate significantly. The correlation function between different rings ($g_{20,50}$) on the other hand, shows that the anisotropic model overestimates the extent of interpenetration of the small within the large rings. For $\rho^* = 10.0$ there is good agreement between the monomer-resolved and the anisotropic effective results for the correlation functions between different rings ($g_{20,50}$) and also between $N = 50$ rings ($g_{50,50}$). The isotropic model on the other hand misses important features for all correlation functions, both for different and identical rings. In the case of the monomer-resolved sim-

ulation, the correlation function between $N = 20$ rings, $g_{20,20}$, exhibits a characteristic peak similar to that observed in the monodisperse system of $N = 20$ rings (figure 7 in ref.[62]). For the anisotropic effective system on the other hand the peak in $g_{20,20}$ is missing at $\rho^* = 10$ and looks similar to the correlation function measured in a monodisperse system of $N = 20$ rings at a lower density. For the higher density, $\rho^* = 15.7$, the peak in $g_{20,20}$ emerges also in the anisotropic effective model, but it is much less pronounced than in the monomer-resolved system at the same density. The peak of the $g_{50,50}$ correlation function at $r \to 0$ is an indication of the formation of clusters, and the corresponding stacks are found both in the anisotropic effective and in the monomer-resolved systems. However, in the monomer-resolved case the peak is much more pronounced and correspondingly also the length of the stacks is increased (see below). Additionally, the $g_{20,50}$ curve exhibits a pronounced peak in the monomer-resolved system for $r \to 0$, which reflects that the clusters are formed both by $N = 50$ and $N = 20$ rings. In the anisotropic effective system this maximum is also visible but much less pronounced, indicating that there are less small rings locked within the columns than in the monomer-resolved system.

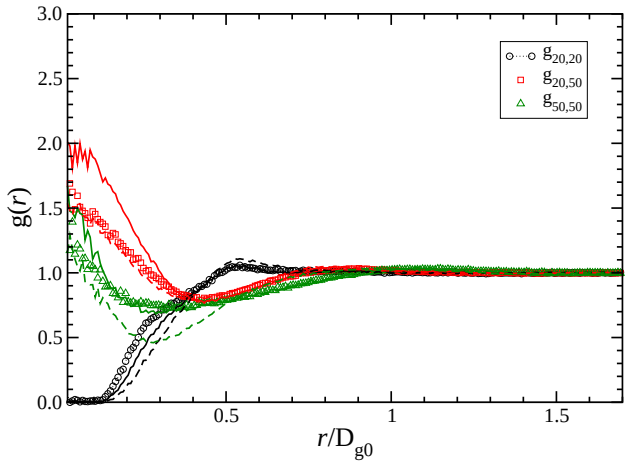

Fig. 9 Pair correlation functions, at density $\rho^* = 3.9$, for the 1:1 mixture, in the full monomer-resolved simulation (symbols), the anisotropic effective model (solid lines) and the isotropic effective model (dashed lines). Different colors refer to the pair correlation function between different types of rings (see legend).

We introduce the function $P(\mathbf{d}^{(1)} \cdot \mathbf{d}^{(2)})$, defined as the probability density distribution for the scalar product between the directors $\mathbf{d}^{(1)}$ and $\mathbf{d}^{(2)}$ of two ring polymers that are separated by a distance $r < 0.6D_{g0}$. Therefore, this function pro-

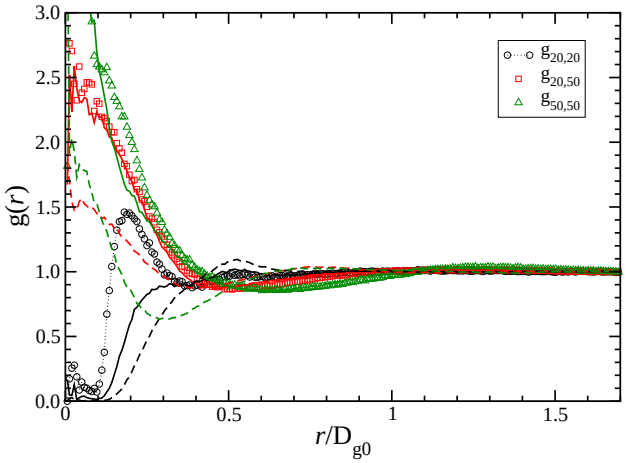

Fig. 10 Pair correlation functions, at density $\rho^* = 10.0$, for the 1:1 mixture, in the full monomer-resolved simulation (symbols), the anisotropic effective model (solid lines) and the isotropic effective model (dashed lines). Different colors refer to the pair correlation function between different types of rings (see legend).

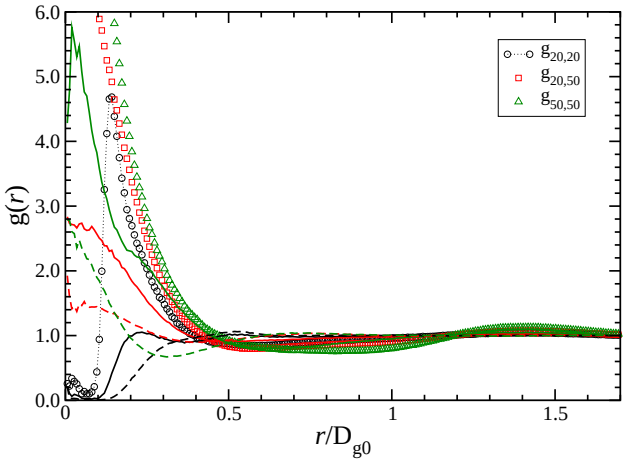

Fig. 11 Pair correlation functions, at density $\rho^* = 15.7$, for the 1:1 mixture, in the full monomer-resolved simulation (symbols), the anisotropic effective model (solid lines) and the isotropic effective model (dashed lines). Different colors refer to the pair correlation function between different types of rings (see legend).

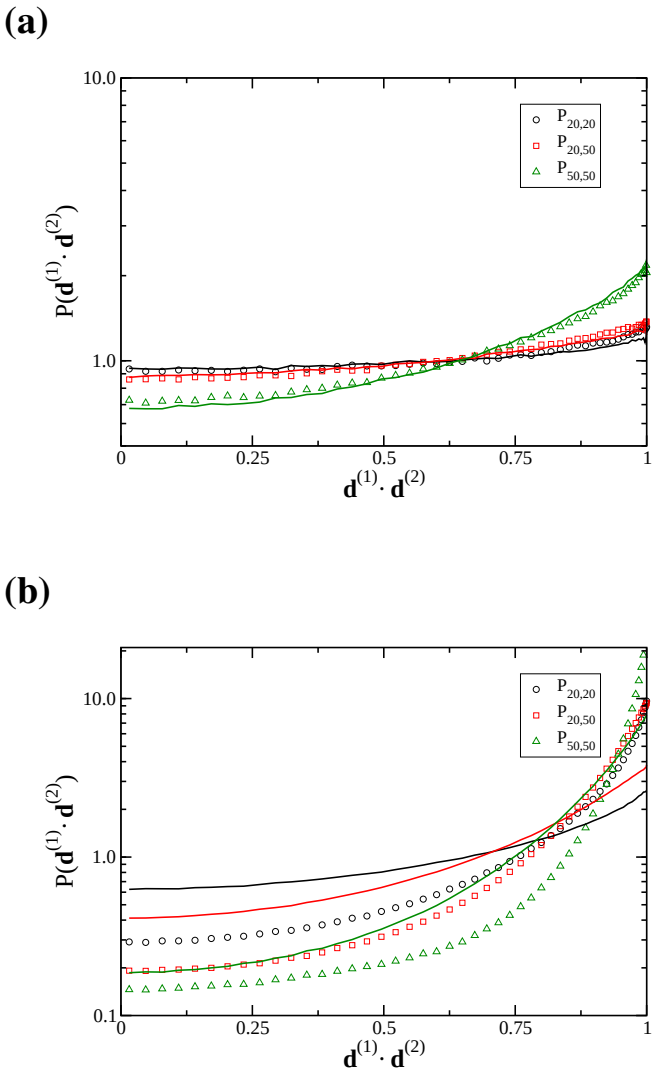

Fig. 12 Probability density $P(\mathbf{d}^{(1)} \cdot \mathbf{d}^{(2)})$ for the scalar product $\mathbf{d}^{(1)} \cdot \mathbf{d}^{(2)}$ between the directors of two close-by rings ($r < 0.6D_{g0}$). The presented results are computed for the 1:1 mixture. Different data sets correspond to distributions for pairs of rings with identical or different N (see legend). Panels **(a)** and **(b)** show results for $\rho^* = 3.9$ and $\rho^* = 15.7$, respectively. Symbols correspond to monomer-resolved simulation data and lines to results obtained in simulations of the effective soft disks.

vides information about orientational correlations in the system. Figure 12 shows the former distribution, computed both for the monomer-resolved system and the anisotropic effective model, at the densities $\rho^* = 3.9$ and 15.7. For the smaller density the anisotropic effective model and the monomer-resolved system are in very good quantitative agreement. For the larger density the rings in the monomer-resolved system are more likely to orient parallel with respect to each other, and correspondingly orthogonal orientations of the directors are largely suppressed. This is consistent with the fact that the large rings in the monomer-resolved system are often part of long stacks, and are therefore almost parallel oriented with respect to each other. We will further elaborate on this in the next section. At the higher density, $\rho^* = 15.7$, the rings in the soft-disk mixture also exhibit an enhanced probability to orient parallel with respect to each other, but while the qualitative behavior is correct, this enhancement is much weaker than in the monomer-resolved case. Correspondingly, we will show in the next section that the rings also form stacks in the anisotropic effective model, though their length is reduced with respect to the monomer-resolved mixture at the same density.

Finally, we also carried out simulations of an asymmetric binary mixture, where 364 chains contained $N = 20$ and the other 1454 rings consisted of $N = 50$ monomers, we will call this system the 1:4 mixture in the following. The partial radial distribution functions for this solution are shown in figure 13 for the representative densities $\rho^* = 11.9$ and 18.6. The qualitative trends of the correlation functions, both for the monomer-resolved and the effective anisotropic model, are the same as those displayed in figure 11 for the symmetric mixture at a similar density $\rho^* = 15.7$. This finding suggests that there is a broad range of compositions in mixtures of small and intermediate rings that will present the qualitative scenario presented above.

8 Formation of Stacks in Binary Mixtures

Finally, we characterize formation of stacks in binary mixtures of rings, to clarify whether monodispersity is a requirement for the formation of long columns, and to test if the anisotropic effective model for mixtures is able to capture the essential features of stacking at high densities. To this end, we have applied the algorithm described in section 3 to identify stacks of the large rings in configurations taken from simulations of the mixtures. First we concentrate on the 1:1 mixture, which contains the same number of rings with $N = 20$ and $N = 50$ monomers.

In figure 14 we show the same configuration of a monomer-resolved simulation at density $\rho^* = 15.7$ in four different representations (see caption). It can be seen that most rings are part of stacks containing 5 or more rings, which are interpenetrated by the small rings. The large rings are not only

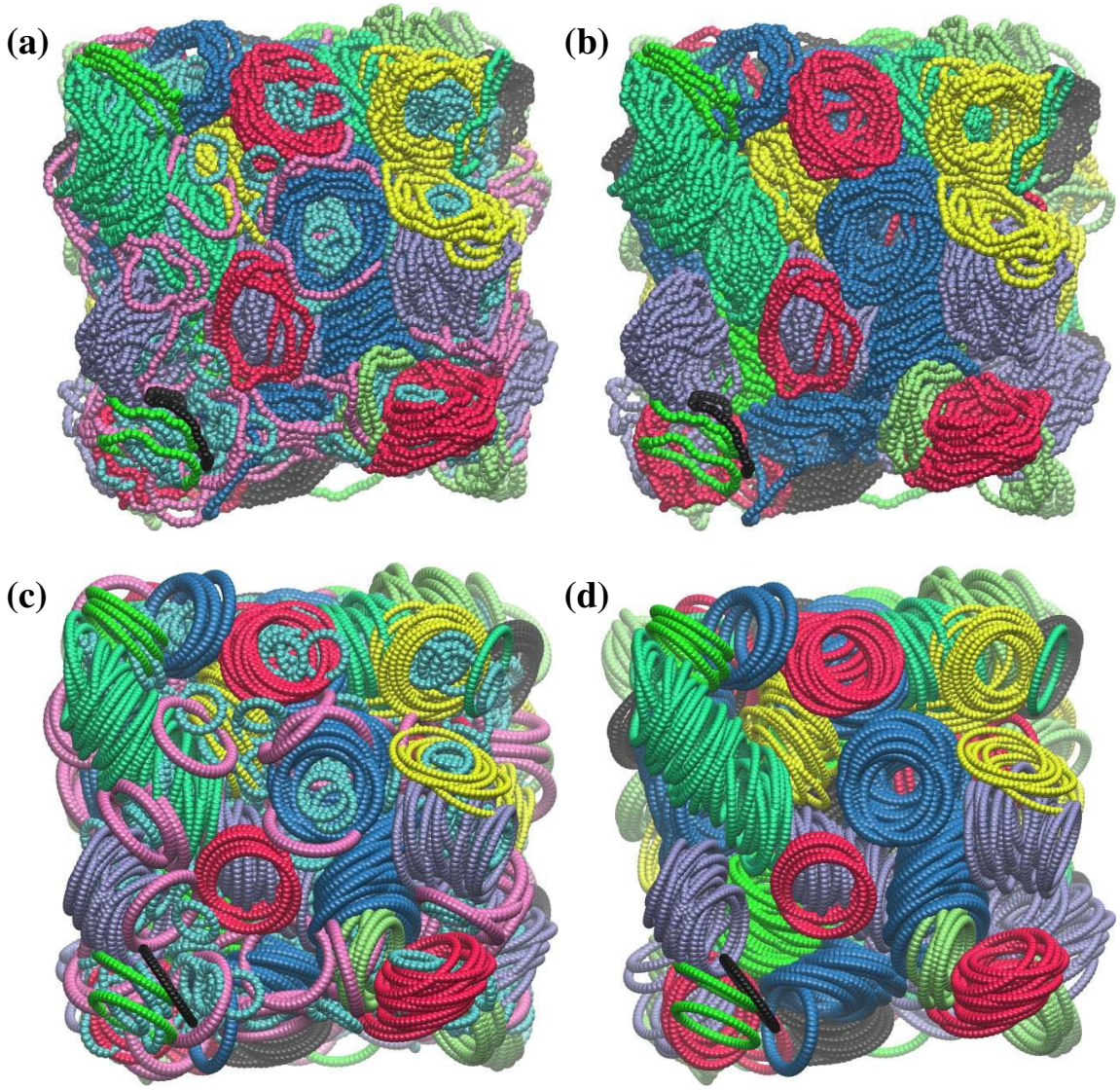

Fig. 14 Visualizations of the same configuration of a monomer-resolved simulation for the 1:1 mixture at density $\rho^* = 15.7$. Large rings which are part of the same stack have identical colors. If the stack has less than 5 members they are colored pink. All small rings are colored turquoise. In **(a)** we show a snapshot with all the rings, while in **(b)** the pink and turquoise rings are not shown. For displaying the snapshots **(c), (d)** we have first computed the effective coordinates (centers-of-mass and directors) of the *monomer-resolved rings* (not to be confused with the soft disks of the simulations of the effective model). Then we have represented the real rings by perfect circles with the same centers-of-mass and directors as the corresponding real rings. Moreover the circles have a radius R_{g0} (different for $N = 20$ and $N = 50$) identical to that of the corresponding real rings at zero density. The representation of the snapshots **(c), (d)** in terms of the effective coordinates facilitates visualization of the internal structure of the stacks. In **(c)** all the rings are displayed. The pink and turquoise rings are not shown in **(d)**.

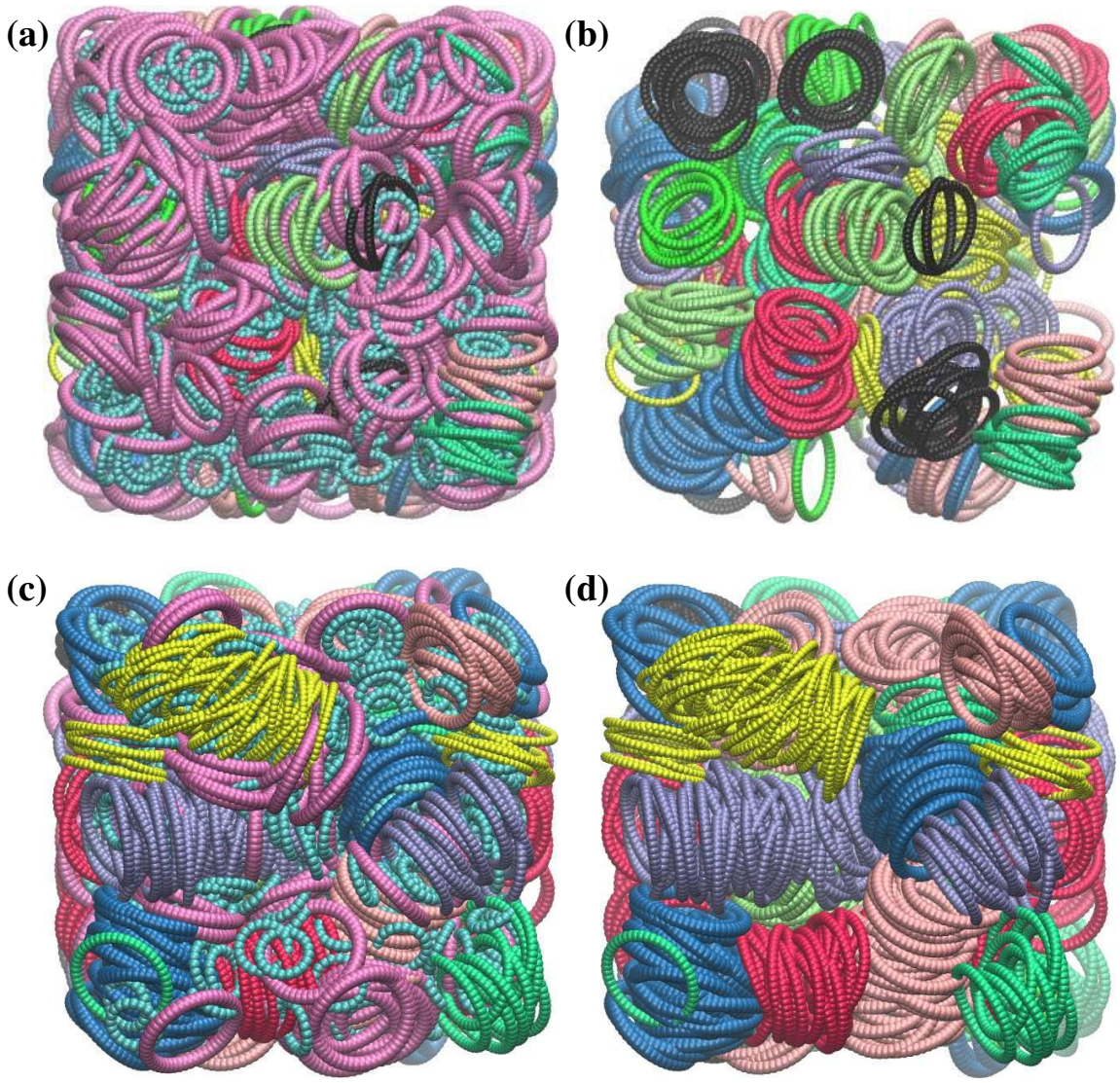

Fig. 15 Snapshots of a simulation of effective soft disks, representing the 1:1 mixture. The effective particles are visualized by perfect circles, with centers-of-mass and directors identical to those of the effective particles. Large rings which are part of the same stack have identical colors. If the stack has less than 5 members they are colored pink. All small rings are colored turquoise. The snapshots **(a), (b)** are taken from a simulation at density $\rho^* = 15.7$, while **(c), (d)** are for the density $\rho^* = 24.9$. The snapshots in **(a), (c)** contain all particles simulated, while the turquoise and pink particles are not shown in **(b), (d)**.

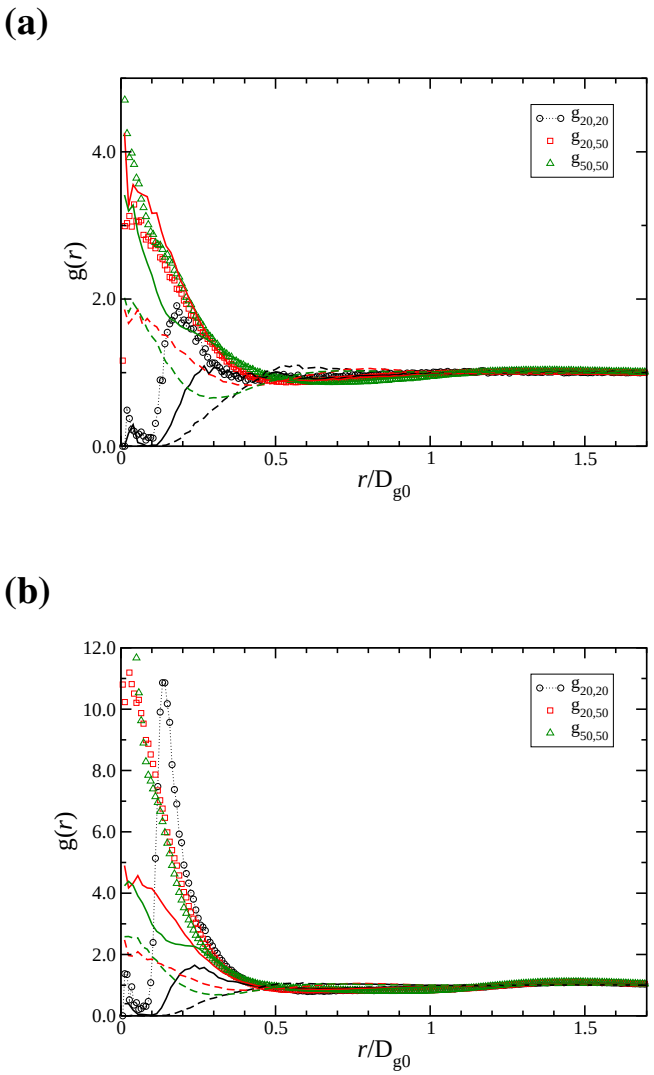

Fig. 13 Pair correlation functions, at densities $\rho^* = 11.9$ **(a)** and 18.6 **(b)**, for the 1:4 mixture in the full monomer-resolved simulation (symbols), the anisotropic effective model (solid lines) and the isotropic effective model (dashed lines). Different colors refer to the pair correlation function between different types of rings (see legend).

parallel with respect to each other, but their centers-of-mass are also aligned, which allows for an unblocked view through the columns if the small rings are not shown and the column stands along your view.

Figure 15 displays configurations of the soft-disk mixture at the densities $\rho^* = 15.7$ and 24.9. We can see that stacks are formed in the anisotropic effective system, but at the same density they are shorter than for the monomer-resolved case. The reason for this could be that the free energy penalty for a small ring which interpenetrates a column is overestimated because the effective potential is pairwise additive and we thus add up contributions due to interactions with many large rings. Analogously, a large ring can be interpenetrated by many small rings and the same interaction penalty is summed up for each additional interpenetration. In the monomer-resolved model on the other hand the free energy penalty could be smaller, since for instance the entropy of a large ring that is interpenetrated by a small one is restricted in first place and it might not reduce by the same amount if a second small ring is locked in. In figure 14, we can indeed see that in the full simulation it is common that large rings are simultaneously pierced by several small rings, while this hardly ever happens in configurations of the effective system displayed in figure 15. By increasing the density in the effective system we eventually encountered systems with a similar probability distribution $\mathrm{P}(n_c)$ as observed in the monomer-resolved simulation at a smaller density. An example of this fact is illustrated in figure 16, where a configuration of the monomer-resolved mixture ($\rho^* = 10.8$) and of the effective soft-disk mixture ($\rho^* = 12.7$) are displayed. In both cases the small rings, as well as large rings not being part of a stack of at least 5 members are not shown. Both snapshots are qualitatively similar. The similarity observed in these snapshots at this and other densities suggests that the anisotropic effective model is at least qualitatively able to reproduce the formation of stacks also for the case of binary mixtures.

Figure 17 shows the probability $\mathrm{P}(n_c)$ for an individual large ring to be part of a stack with n_c members. As in the monodisperse case, we find that for a given monomer-resolved system there exists an effective soft-disk system, at a higher density, with a similar stack size distribution. The formation of stacks is typically accompanied by a high maximum at $r \to 0$ in the radial distribution function of the large rings. This can be seen in figure 18 where we plot this correlation function for the monomer-resolved and the anisotropic effective models. While the maximum is lower in the soft-disk model than in the monomer-resolved one, it also increases with the density.

Finally, we have also characterized stacks in simulations of the 1:4 mixture. Figure 19 shows two representations of the same configuration, for density $\rho^* = 18.6$, of the monomer-resolved 1:4 mixture. We can see that the system still forms

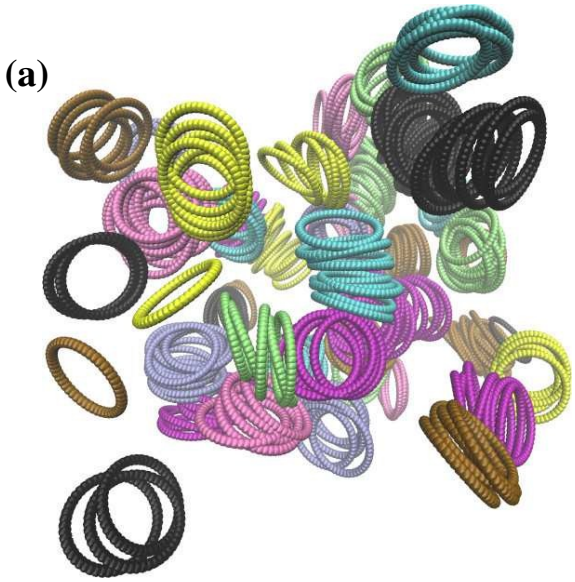

Fig. 16 Snapshot **(a)** represents a visualization of the effective degrees of freedom in a configuration taken from a monomer-resolved simulation at density $\rho^* = 10.8$, while **(b)** represents a configuration from a simulation of the anisotropic effective model at $\rho^* = 12.7$. In both cases the small rings, as well as large rings which are not part of a stack with at least 5 members, are not shown.

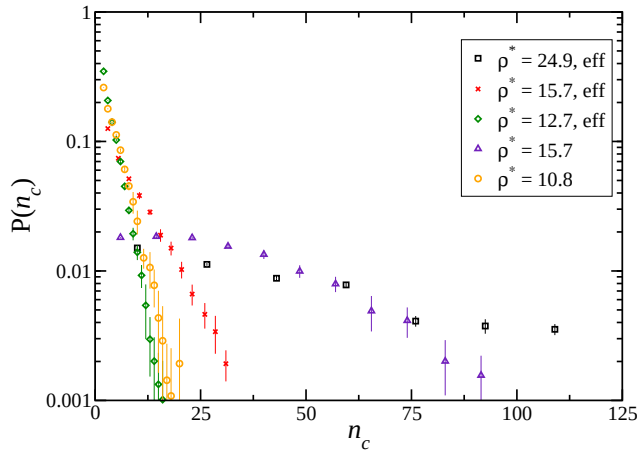

Fig. 17 Probability distribution, P(n_c), for a large ring to be part of a stack with n_c members, in simulations of the 1:1 mixture.

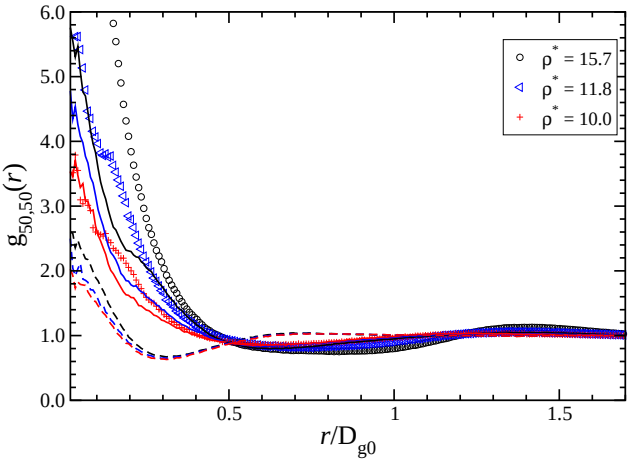

Fig. 18 Radial pair distribution function of the large rings for a simulation of the 1:1 mixture. Data is shown for the monomer-resolved simulation (symbols), the anisotropic effective model (solid lines) and the isotropic effective model (dashed lines).

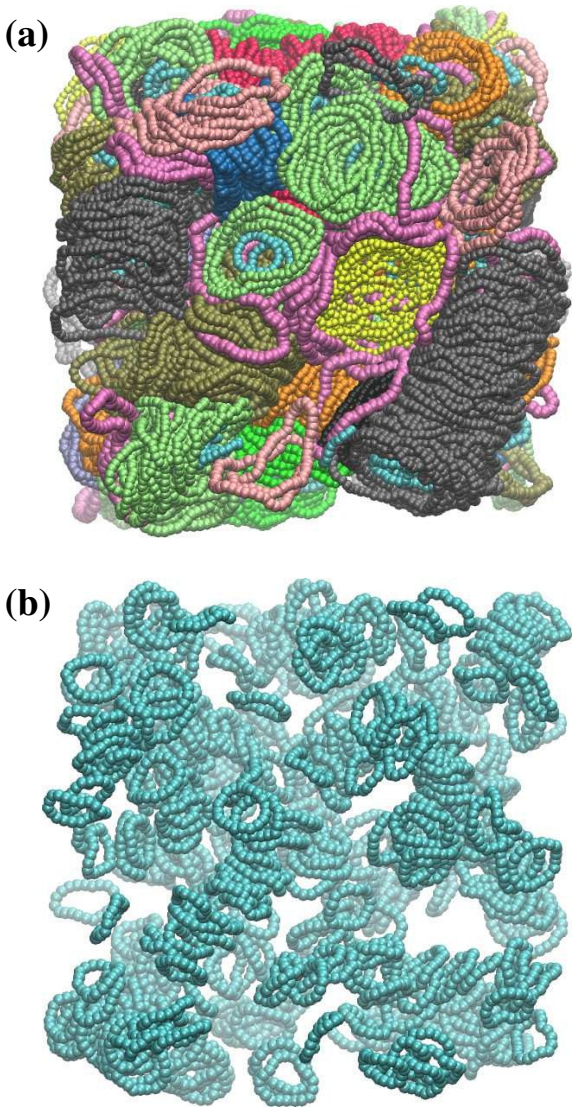

Fig. 19 Visualizations of a configuration from a monomer-resolved simulation of the 1:4 mixture at density $\rho^* = 18.6$. In **(a)** we show a snapshot with all the rings, while in **(b)** only the small rings are shown.

long columns of large rings penetrated by small ones. In snapshot 19a all the rings are displayed, while in 19b only the small rings are shown. Interestingly, the small rings do not fill all the columns formed by the large ones. Moreover, the columns in which the small rings are present are not filled homogeneously; the small rings agglomerate within some tubes formed by the large rings, while others remain hollow of small rings. This agglomeration is consistent with the sharp peak observed in the radial distribution function of the small rings $g_{20,20}$ (see figure 13 above). The fact that the small rings aggregate within the large rings could mean that the free energy penalty of many small rings interpenetrating a few large ones is smaller than that of many large rings being interpenetrated by individual small rings. This interpretation is also consistent with the reduced amount of interpenetration observed in the anisotropic effective model. This only includes pair interactions and therefore does not take into account that, for the real rings, the energy penalty of inserting an additional small ring inside a large one is not necessarily identical to the free energy penalty due to the interpenetration of the first small ring. A snapshot of the asymmetric effective soft-disk mixture at the former density $\rho^* = 18.6$ is displayed in figure 20. Again, columns are formed in the effective system but the stacks are smaller than in the monomer-resolved case. Finally, figure 21 shows the probability distribution $P(n_c)$ for the asymmetric mixtures in the monomer-resolved and effective soft-disk models. We find the same qualitative features as in figure 17 for the symmetric mixtures.

9 Conclusions

We have presented extensive simulations of concentrated solutions of semiflexible ring polymers. These systems form phases containing columnar, tube-like structures of quasi-parallel rings (stacks). This feature, which cannot be captured by the standard isotropic effective interactions, is qualitatively reproduced by an anisotropic effective model. In this model the effective interactions do not only depend on the distance between macromolecular centers-of-mass, but also on the relative orientations. We have introduced a simple algorithm to identify and characterize the stacks. Though, for the same density, the stacks are longer in the monomer-resolved system than in the effective anisotropic model, long stacks can be formed in both models at sufficiently high concentrations. The anisotropic model is, in general, clearly superior to the isotropic model. However, in ref.[62] it was shown that, for semiflexible rings with a significant degree of deformability, the isotropic effective model provided a better description of the real system than the anisotropic model in the range of density investigated there. This was attributed to the overestimation of the orientational effects in the interactions between such deformable rings. However, by further increasing the

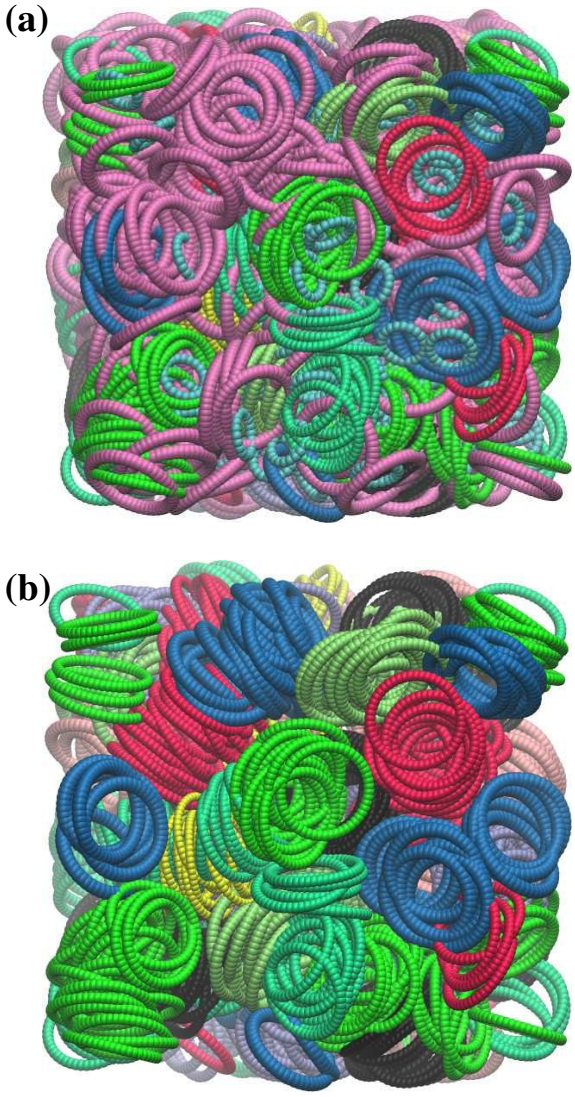

Fig. 20 Snapshots of a simulation of effective soft disks, representing the 1:4 mixture at density $\rho^* = 18.6$. The effective particles are visualized by perfect circles with centers-of-mass and directors identical to those of the corresponding effective particles. The snapshot in **(a)** displays all particles simulated. The small rings (turquoise), as well as the large rings that are not part of a stack with at least 5 members (pink), are not shown in **(b)**.

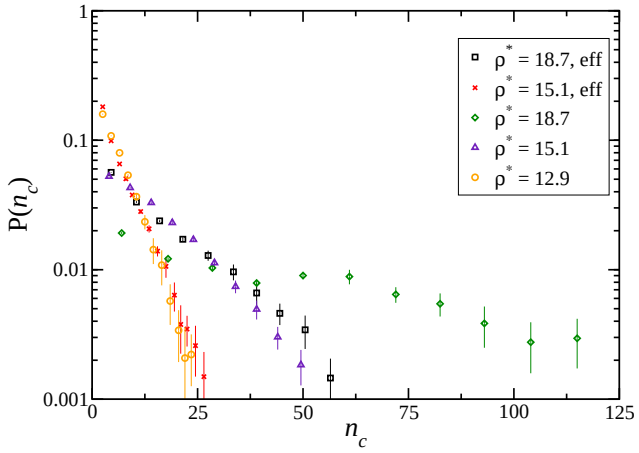

Fig. 21 Probability distribution, $P(n_c)$, for a large ring to be part of a stack with n_c members in simulations of the 1:4 mixture.

density, we have found that such rings expand themselves to optimize packing, stacks are formed and the anisotropic model provides again a superior description over the isotropic model.

We have extended the effective model to the case of binary mixtures of ring polymers, and compared it with simulations of the corresponding monomer-resolved mixtures. The simulations reveal stack formation in both models for a broad range of mixture compositions, demonstrating that stacking is highly resilient to polydispersity. As expected, the stacks in asymmetric mixtures are mostly constituted by columns of large rings. The small rings tend to be located inside of such columns. However, they do not fill them homogeneously but form agglomerates within the columns.

Acknowledgments

This work has been supported by the Austrian Science Fund (FWF), Grant 23400-N16. We acknowledge allocation of CPU time in CSUC (Spain).

References

1 M. Rubinstein and R. Colby, *Polymer Physics*, Oxford University Press, Oxford, 2003.
2 J. Des Cloizeaux, *J. Phys. (Paris)*, 1981, **42**, 635–652.
3 A. Y. Grosberg, A. Feigel and Y. Rabin, *Phys. Rev. E*, 1996, **54**, 6618.
4 J. Deutsch, *Phys. Rev. E*, 1999, **59**, R2539.

5 A. Y. Grosberg, *Phys. Rev. Lett.*, 2000, **85**, 3858.

6 A. Dobay, J. Dubochet, K. Millett, P.-E. Sottas and A. Stasiak, *Proc. Nat. Acad. Sci. USA*, 2003, **100**, 5611–5615.

7 N. T. Moore, R. C. Lua and A. Y. Grosberg, *Proc. Nat. Acad. Sci. USA*, 2004, **101**, 13431–13435.

8 N. T. Moore and A. Y. Grosberg, *Phys. Rev. E*, 2005, **72**, 061803.

9 M. L. Mansfield and J. F. Douglas, *J. Chem. Phys.*, 2010, **133**, 044903.

10 T. Vettorel, A. Y. Grosberg and K. Kremer, *Phys. Biol.*, 2009, **6**, 025013.

11 J. D. Halverson, W. B. Lee, G. S. Grest, A. Y. Grosberg and K. Kremer, *J. Chem. Phys.*, 2011, **134**, 204904.

12 S. Y. Reigh and D. Y. Yoon, *ACS Macro Letters*, 2013, **2**, 296–300.

13 M. Kapnistos, M. Lang, D. Vlassopoulos, W. Pyckhout-Hintzen, D. Richter, D. Cho, T. Chang and M. Rubinstein, *Nature Materials*, 2008, **7**, 997–1002.

14 J. D. Halverson, W. B. Lee, G. S. Grest, A. Y. Grosberg and K. Kremer, *J. Chem. Phys.*, 2011, **134**, 204905.

15 R. Pasquino, T. C. Vasilakopoulos, Y. C. Jeong, H. Lee, S. Rogers, G. Sakellariou, J. Allgaier, A. Takano, A. R. Brs, T. Chang, S. Gooen, W. Pyckhout-Hintzen, A. Wischnewski, N. Hadjichristidis, D. Richter, M. Rubinstein and D. Vlassopoulos, *ACS Macro Letters*, 2013, **2**, 874–878.

16 D. Richter, S. Goossen and A. Wischnewski, *Soft Matter*, 2015, **11**, 8535–8549.

17 M. Bohn and D. W. Heermann, *J. Chem. Phys.*, 2010, **132**, 044904.

18 D. Marenduzzo and E. Orlandini, *JSTAT: Theory and Experiment*, 2009, **2009**, L09002.

19 J. Dorier and A. Stasiak, *Nucl. Acids Res.*, 2009, **37**, 6316–6322.

20 D. Marenduzzo, C. Micheletti and E. Orlandini, *J. Phys.: Condens. Matter*, 2010, **22**, 283102.

21 A. Rosa, *Biochem. Soc. Trans.*, 2013, **41**, 612–615.

22 J. D. Halverson, J. Smrek, K. Kremer and A. Y. Grosberg, *Rep. Progr. Phys.*, 2014, **77**, 022601.

23 C. N. Likos, *Soft Matter*, 2006, **2**, 478–498.

24 A. Louis, P. Bolhuis, J. Hansen and E. Meijer, *Phys. Rev. Lett.*, 2000, **85**, 2522.

25 V. Krakoviack, J.-P. Hansen and A. Louis, *Phys. Rev. E*, 2003, **67**, 041801.

26 A. Narros, C. N. Likos, A. J. Moreno and B. Capone, *Soft Matter*, 2014, **10**, 9601–9614.

27 C. N. Likos, H. Löwen, M. Watzlawek, B. Abbas, O. Jucknischke, J. Allgaier and D. Richter, *Phys. Rev. Lett.*, 1998, **80**, 4450.

28 A. Jusufi and C. N. Likos, *Rev. Mod. Phys.*, 2009, **81**, 1753.

29 D. Marzi, C. N. Likos and B. Capone, *J. Chem. Phys.*, 2012, **137**, 014902.

30 B. Capone, I. Coluzza, F. LoVerso, C. N. Likos and R. Blaak, *Phys. Rev. Lett.*, 2012, **109**, 238301.

31 A. Jusufi, C. N. Likos and H. Löwen, *J. Chem. Phys.*, 2002, **116**, 11011–11027.

32 S. Huißmann, R. Blaak and C. N. Likos, *Macromolecules*, 2009, **42**, 2806–2816.

33 M. Ballauff and C. N. Likos, *Angew. Chem. Int. Ed.*, 2004, **43**, 2998–3020.

34 I. O. Götze, H. M. Harreis and C. N. Likos, *J. Chem. Phys.*, 2004, **120**, 7761–7771.

35 S. Huißmann, C. N. Likos and R. Blaak, *Soft Matter*, 2011, **7**, 8419–8427.

36 C. Pierleoni, C. Addison, J.-P. Hansen and V. Krakoviack, *Phys. Rev. Lett.*, 2006, **96**, 128302.

37 C. Pierleoni, B. Capone and J.-P. Hansen, *J. Chem. Phys.*, 2007, **127**, 171102.

38 B. Capone, C. Pierleoni, J.-P. Hansen and V. Krakoviack, *J. Phys. Chem. B*, 2008, **113**, 3629–3638.

39 A. Narros, A. J. Moreno and C. N. Likos, *Soft Matter*, 2010, **6**, 2435–2441.

40 M. Bernabei, P. Bacova, A. J. Moreno, A. Narros and C. N. Likos, *Soft Matter*, 2013, **9**, 1287–1300.

41 F. Ferrari and I. Lazzizzera, *Nucl. Phys. B*, 1999, **559**, 673–688.

42 A. Narros, A. J. Moreno and C. N. Likos, *Macromolecules*, 2013, **46**, 9437–9445.

43 C. N. Likos, *Phys. Rep.*, 2001, **348**, 267–439.

44 F. H. Stillinger, *J. Chem. Phys.*, 1976, **65**, 3968–3974.

45 A. Lang, C. N. Likos, M. Watzlawek and H. Löwen, *Journal of Physics: Condensed Matter*, 2000, **12**, 5087.

46 S. Prestipino, F. Saija and P. V. Giaquinta, *Phys. Rev. E*, 2005, **71**, 050102.

47 J. C. Pàmies, A. Cacciuto and D. Frenkel, *J. Chem. Phys.*, 2009, **131**, 044514.

48 L. Berthier, A. J. Moreno and G. Szamel, *Phys. Rev. E*, 2010, **82**, 060501.

49 A. Ikeda and K. Miyazaki, *Phys. Rev. Lett.*, 2011, **106**, 015701.

50 D. Paloli, P. S. Mohanty, J. J. Crassous, E. Zaccarelli and P. Schurtenberger, *Soft Matter*, 2013, **9**, 3000–3004.

51 B. M. Mladek, D. Gottwald, G. Kahl, M. Neumann and C. N. Likos, *Phys. Rev. Lett.*, 2006, **96**, 045701.

52 A. J. Moreno and C. N. Likos, *Phys. Rev. Lett.*, 2007, **99**, 107801.

53 S. van Teeffelen, A. J. Moreno and C. N. Likos, *Soft Matter*, 2009, **5**, 1024–1038.

54 Y.-L. Zhu and Z.-Y. Lu, *J. Chem. Phys.*, 2011, **134**, 044903.

55 D. Coslovich, M. Bernabei and A. J. Moreno, *J. Chem. Phys.*, 2012, **137**, 184904.

56 D. A. Lenz, R. Blaak, C. N. Likos and B. M. Mladek, *Phys. Rev. Lett.*, 2012, **109**, 228301.

57 A. J. Archer, A. M. Rucklidge and E. Knobloch, *Phys. Rev. Lett.*, 2013, **111**, 165501.

58 F. Sciortino and E. Zaccarelli, *Nature*, 2013, **493**, 30–31.

59 D. Coslovich and A. Ikeda, *Soft Matter*, 2013, **9**, 6786–6795.

60 K. Barkan, M. Engel and R. Lifshitz, *Phys. Rev. Lett.*, 2014, **113**, 098304.

61 M. Z. Slimani, P. Bacova, M. Bernabei, A. Narros, C. N. Likos and A. J. Moreno, *ACS Macro Lett.*, 2014, **3**, 611–616.

62 P. Poier, C. N. Likos, A. J. Moreno and R. Blaak, *Macromolecules*, 2015, **48**, 4983–4997.

63 A. Rosa, E. Orlandini, L. Tubiana and C. Micheletti, *Macromolecules*, 2011, **44**, 8668–8680.

64 T. Heinemann, K. Palczynski, J. Dzubiella and S. H. Klapp, *J. Chem. Phys.*, 2014, **141**, 214110.

65 T. Heinemann, K. Palczynski, J. Dzubiella and S. H. Klapp, *J. Chem. Phys.*, 2015, **143**, 174110.

66 K. Kremer and G. S. Grest, *J. Chem. Phys.*, 1990, **92**, 5057–5086.

67 S. Mossa, F. Sciortino, P. Tartaglia and E. Zaccarelli, *Langmuir*, 2004, **20**, 10756–10763.

68 F. Sciortino, S. Mossa, E. Zaccarelli and P. Tartaglia, *Phys. Rev. Lett.*, 2004, **93**, 055701.

Fig. 22 TOC figure: Binary mixtures of semiflexible ring polymers form stacks at high densities.